

RSC Advances



This is an *Accepted Manuscript*, which has been through the Royal Society of Chemistry peer review process and has been accepted for publication.

Accepted Manuscripts are published online shortly after acceptance, before technical editing, formatting and proof reading. Using this free service, authors can make their results available to the community, in citable form, before we publish the edited article. This *Accepted Manuscript* will be replaced by the edited, formatted and paginated article as soon as this is available.

You can find more information about *Accepted Manuscripts* in the [Information for Authors](#).

Please note that technical editing may introduce minor changes to the text and/or graphics, which may alter content. The journal's standard [Terms & Conditions](#) and the [Ethical guidelines](#) still apply. In no event shall the Royal Society of Chemistry be held responsible for any errors or omissions in this *Accepted Manuscript* or any consequences arising from the use of any information it contains.

Organic mediated synthesis of highly luminescent Li⁺ ion compensated Gd₂O₃:Eu³⁺ nanophosphors and its Judd-Ofelt analysis

R. G. Abhilash Kumar,^{a,b} Satoshi Hata,^c Ken-ichi Ikeda,^d and K. G. Gopchandran^{a,*}

^aDepartment of Optoelectronics, University of Kerala, Thiruvananthapuram- 695 581, India

^bDepartment of Physics, University College, Thiruvananthapuram- 695 034, India

^cDepartment of Electrical and Materials Science, Faculty of Engineering Sciences, Kyushu University, Kasuga, Fukuoka 816-8580, Japan

^dDivision of Materials Science and Engineering, Faculty of Engineering, Hokkaido University, Kita13, Nishi8, Kita-ku, Sapporo, Hokkaido 060-8628, Japan

*Corresponding author.

Tel.: +914712308167

Email: gopchandran@yahoo.com

Abstract

Highly luminescent red emitting Gd₂O₃:Eu³⁺, Li⁺ nanophosphor has been synthesized by the solvothermal combustion of metal-citrate complex in diethylene glycol medium. The morphology and luminescent properties of these nanophosphors are found to be highly sensitive to the extent of lithium ion compensation. It is found that lithium ions promote grain growth and alter the morphology of Gd₂O₃:Eu³⁺ nanophosphor from nearly spherical to cobblestone like. A significant enhancement in intensity of luminescence and quantum efficiency is observed in lithium compensated nanophosphors. The highest emission intensity is observed for the Gd_{1.75}Eu_{0.1}Li_{0.15}O₃ nanophosphor, about 1.83 times that of Gd_{1.9}Eu_{0.1}O₃ and is attributed to the enhanced intra 4f-4f emission transitions arising from the modifications of the crystal field and distortion of the local symmetry around the europium ions. The luminescence decay profiles are found to be single exponential in nature and the lifetime measured was 1.36 ms for the Gd_{1.75}Eu_{0.1}Li_{0.15}O₃ nanophosphor. The chromaticity coordinates of these nanophosphors indicated high colour purity. Judd-Ofelt intensity parameters indicated that lithium compensation increases the polarization of the local environment and an increase of covalency and asymmetry around the europium ions.

1. Introduction

Investigations on rare earth based inorganic nanophosphors attracted significant scientific interest because of the excellent emission features and their tremendous demand for potential applications in displays, lighting, lasers, optical communication, finger print sensing, bio-labels and bio-imaging.¹ Inorganic luminescent materials with long-term stability, enhanced brightness, faster response and better quantum efficiency are needed to meet the requirements of these devices. In this direction, extensive research has been carried out on rare earth ion activated oxide based phosphors, which is motivated by their excellent colour purity, long chemical durability, lack of photobleaching and high thermal stability. The 4f-4f electronic transitions of rare earth ions produce narrow emissions with relatively long lifetime, which is due to the shielding effect of its partially filled 4f-shell electrons by the filled 5s and 5p electrons.² The intensity, colour purity and quantum efficiency of the emission transitions from the rare earth activators depend on the nature of the host, interaction between the rare earth ions and the host, symmetry around the activator, concentration and distribution of activator ions and the effectiveness of energy transfer from the host or sensitizer to the activators.¹

Trivalent rare earth ions such as Eu^{3+} , Tb^{3+} , Sm^{3+} , Er^{3+} , Tm^{3+} and Ho^{3+} can act as excellent luminescent centres in inorganic phosphors because of their rich electronic energy levels for radiative transitions and their suitability of excitation in the ultraviolet, visible and near infrared regions. Among the different rare earth ions, trivalent Eu^{3+} activated phosphors are technologically important for photonic applications due to the simple energy level structure of Eu^{3+} ions, which produce intense, narrow red emissions by the intra 4f-4f $^5\text{D}_0$ - $^7\text{F}_J$ ($J=0$ to 6) optical transitions. Suitable host material for the rare earth ions should possess large optical band gap combined with good thermal and chemical stability. In order to improve the luminescence from Eu^{3+} , it should be incorporated into host materials having low phonon energy. Gadolinium oxide (Gd_2O_3), a rare earth sesquioxide can perform as an excellent luminescent host material for the rare earth ions because of its better chemical durability, good thermal stability, high density, ability of easy incorporation with rare earth ions, high refractive index and low phonon energy of 600 cm^{-1} .³⁻⁸ Moreover, the ionic radius of Eu^{3+} (0.0947 nm) is close to that of Gd^{3+} (0.0938 nm), which makes the incorporation of Eu^{3+} into the host lattice, Gd_2O_3 easier. $\text{Gd}_2\text{O}_3:\text{Eu}^{3+}$ is a paramagnetic efficient red emitting phosphor that has been widely employed in fluorescent lamps, lighting, photonic displays, security inks, cathode-ray tubes, contrast agent in magnetic resonance imaging and bio-related applications.^{1,9-11} At lower temperature, Gd_2O_3 crystallizes in the cubic bixbyite

structure (space group: Ia-3 (206), Th⁷) and two distinct cationic sites are available for the rare earth ions - a non-centrosymmetric site, C₂ and a centrosymmetric site, S₆ with an occupancy ratio of 3:1. The occupancy of Eu³⁺ ions in these sites is reflected in the luminescent and radiative properties of the synthesized phosphors.

The intra 4f-4f electronic transitions of Eu³⁺ ions are strongly dependent on the crystal structure of the host and are sensitive to the local structural environment around it. When Eu³⁺ is located at a non-centrosymmetric site, it can generate high quality red emission corresponding to the ⁵D₀-⁷F₂ electronic transition. Recent studies by several groups have revealed that the incorporation of rare earth ions together with alkali metal ions in host matrices can effectively enhance the emission intensity and quantum efficiency of nanophosphors. Alkali metal ions can distort the host lattice, alter the host-activator interactions, modify the energy absorption and transfer behaviours, inducing enhancement of emission properties. Moreover, alkali metal ions can play a crucial role to control the crystallinity and morphology of the nanophosphors. The alkali metal, lithium (Li⁺) ion has the least cationic radius making both its movement and site occupation substitutionally or interstitially in the host lattice easier, which will reduce the symmetry of the crystal field around the Eu³⁺ activators and results in enhanced emission properties. Several groups have studied the effect of monovalent lithium (Li⁺) incorporation on the structure, morphology and luminescence properties of YBO₃:Eu³⁺,¹² Y₂O₃:Eu³⁺,¹³⁻¹⁵ Gd₂O₃:Eu³⁺,¹⁶⁻¹⁹ GdVO₄:Eu³⁺,²⁰ YVO₄:Eu³⁺,²¹ YNbTiO₆:Eu³⁺,²² SrTiO₃:Pr³⁺,²³ CaTiO₃:Eu³⁺,²⁴ and BaMoO₄:Sm³⁺,²⁵ phosphors. These studies indicated the importance of evaluating the luminescence dynamics of lithium compensated rare earth based inorganic phosphors for practical applications. In the Li⁺ compensated Gd₂O₃:Eu³⁺ nanophosphors, Li⁺ is employed to act as a flux as well as a sensitizer of luminescence by reducing the symmetry around the Eu³⁺ activators.

Solution combustion synthesis is a versatile, simple, cost effective rapid process to prepare a variety of nanosized materials. Recently, we have successfully synthesized Gd₂O₃:Eu³⁺ nanophosphors by the controlled solvothermal combustion in diethylene glycol medium.^{26,27} Motivated by the attempts to develop efficient phosphors herein, synthesis of highly luminescent lithium compensated red emitting cubic Gd_{1.9-x}Eu_{0.1}Li_xO₃ (x = 0, 0.05, 0.1, 0.15 and 0.2) nanophosphor by the solvothermal combustion of metal-citrates in diethylene glycol is reported. Possible reasons for the considerable enhancement in photoluminescence emission intensity by the incorporation of Li⁺ are discussed in detail. The compensation of lithium with ionic radius and charge states different from that of the host Gd³⁺ ions produced a remarkable effect on the growth process, crystallinity and crystal

symmetry around the Eu^{3+} ions. A comprehensive investigation on the optical spectroscopy and luminescence dynamics of $\text{Gd}_2\text{O}_3:\text{Eu}^{3+}$, Li^+ was done from the emission spectrum by evaluating the Judd-Ofelt and radiative parameters.

2. Experimental

$\text{Gd}_{1.9-x}\text{Eu}_{0.1}\text{Li}_x\text{O}_3$ ($x = 0, 0.05, 0.1, 0.15$ and 0.2) nanophosphors were synthesized by the solvothermal combustion of metal-citrate complex in diethylene glycol. The starting materials used were gadolinium oxide (Gd_2O_3 , 99.99%, Aldrich), europium oxide (Eu_2O_3 , 99.99%, Aldrich), lithium nitrate (LiNO_3 , 99.9%, Merck), polyethylene glycol 200 (PEG, 99%, Merck), diethylene glycol (DEG, $\text{C}_4\text{H}_{10}\text{O}_3$, Merck, 99%), conc. HNO_3 (70%, Merck) and citric acid monohydrate ($\text{C}_6\text{H}_8\text{O}_7 \cdot \text{H}_2\text{O}$). Stoichiometric amounts of Eu_2O_3 , Gd_2O_3 and LiNO_3 corresponding to the composition $\text{Gd}_{1.9-x}\text{Eu}_{0.1}\text{Li}_x\text{O}_3$ ($x = 0, 0.05, 0.1, 0.15$ and 0.2) were weighed separately. Of these, Eu_2O_3 and Gd_2O_3 were dissolved in concentrated nitric acid and deionized water to prepare their fresh nitrate solutions and LiNO_3 is dissolved in deionized water. All the initial nitrate solutions were then homogeneously mixed by magnetic stirring and citric acid in diethylene glycol (citric acid to metal nitrates molar ratio as 2:1) was added drop-wise to the mixed nitrate solution to chelate the metal ions and to initiate the formation of metal-citrate complex. Consequently, about 2 ml of PEG is also added to this solution as a mineraliser. This homogeneously mixed solution was then kept at $\sim 100^\circ\text{C}$ in a water bath with continuous stirring until a highly transparent viscous solution is resulted. This viscous solution is then placed in a muffle furnace at 180°C for one hour and then subjected to combustion at 400°C . The well ground precursor powder was then subjected to heat treatment in a muffle furnace at 800°C for 2 h to obtain the $\text{Gd}_{1.9-x}\text{Eu}_{0.1}\text{Li}_x\text{O}_3$ nanophosphors.

X-ray diffraction (XRD) measurements were carried out on a X'pert Pro X-ray diffractometer (Philips PANalytical, Ni filtered $\text{CuK}\alpha$: 1.54056 \AA , 40 kV, 30 mA) scanning in the 10 to $60^\circ 2\theta$ range, employing X'Celerator and monochromator at the diffracted beam side. Low and high resolution transmission electron microscopy (TEM) were performed in a FEI Tecnai F20 electron microscope having a field emission gun operating at 200 kV and the images were collected digitally using a Gatan multipole CCD camera. Diffuse reflectance (DRS) measurements were recorded using a UV-visible spectrophotometer (JASCO V550) coupled with an integrating sphere attachment (ISV-469) and BaSO_4 is used as the reference for measurements. Raman studies were performed on a confocal microRaman spectrometer (Horiba Jobin-Yvon LABRAM-HR800) in the backscattering geometry with a 785 nm semiconductor diode laser (current of 198 mA) and employing a peltier cooled CCD detector.

Photoluminescence emission and excitation spectra were recorded on a Jobin-Yvon Horiba Fluorolog (FL3-11) spectrofluorometer equipped with a 450W Xenon lamp as the excitation source and a photomultiplier tube in photon counting mode (Hamamatsu R928P) as the detector. Lifetimes were measured by 'decay by delay method' using a phosphorimeter (FL-1040) connected to the spectrofluorometer and equipped with a microsecond pulsed xenon lamp as the excitation source. The CIE chromaticity coordinates (x , y) and correlated colour temperature (CCT) of the nanophosphors were determined from the emission spectra using the 1931 Commission Internationale de l'Eclairage (CIE) 2° colour matching functions as the basis. Photoluminescent emission spectra and transient luminescence decay curves were used to evaluate the Judd-Ofelt intensity and radiative parameters of the synthesized phosphors.

3. Results and discussion

3.1 Phase analysis, crystal structure and morphology studies

X-ray diffraction technique was used to analyse the phase formation, crystal structure, crystallinity and crystallite size of the samples. Fig. 1 shows the X-ray diffraction (XRD) patterns of $\text{Gd}_{1.9-x}\text{Eu}_{0.1}\text{Li}_x\text{O}_3$ nanophosphors as a function of Li^+ content. All the diffraction peaks are indexed according to the cubic bixbyite structure of Gd_2O_3 (JCPDS File No.12-0797) system. No secondary phase of europium or lithium is detected indicating that Li^+ and Eu^{3+} are completely compensated in the Gd_2O_3 host lattice and does not cause any significant change to the crystal structure. However, with increase in lithium content, diffraction peaks are shifted to higher 2θ values indicating slight decrease in lattice parameters and cell volume due to the probable substitution of Li^+ (ionic radius = 0.076 nm with a co-ordination of 6) in Gd^{3+} (ionic radius = 0.0938 nm with a co-ordination of 6) lattice sites. Also from the figure, it can be seen that the diffraction peak intensities increase and the width decrease with increase of Li^+ content. This indicates that lithium acts as a self-promoting or flux agent for the growth of phosphors, consequently crystallinity and grain size get improved. The crystallite size (D) of the phosphors was determined from the diffraction data using the Debye-Scherrer equation²⁸

$$\text{Crystallite size } (D) = \frac{K\lambda}{\beta_{hkl} \cos\theta_{hkl}} \quad (1)$$

where ' λ ' is the wavelength of $\text{CuK}\alpha$ X-rays used (0.154056 nm), β is the full width at half maximum (FWHM) of the diffraction peaks in radian, θ is the Bragg diffraction angle, D_{hkl} represents the size along the specified ($h k l$) direction and K is a constant (nearly equal to 0.9). Fig. 2 depicts the variation of lattice constant, cell volume and crystallite size of the

phosphors as a function of lithium content. It is found that the lattice constant and cell volume of $\text{Gd}_2\text{O}_3:\text{Eu}^{3+}$ samples decrease and the crystallite size increases with increase of Li^+ content.

The morphology, grain size and lattice spacing of the phosphors were investigated by the low and high resolution transmission electron microscopic techniques. Fig. 3 (a-c) and 3 (d-f) present the typical TEM and selected area electron diffraction (SAED) patterns of $\text{Gd}_{1.9}\text{Eu}_{0.1}\text{O}_3$ and $\text{Gd}_{1.75}\text{Eu}_{0.1}\text{Li}_{0.15}\text{O}_3$ nanophosphors, respectively. Both the TEM images indicate that the synthesized nanophosphor is highly homogeneous in size and shape with diameters of about 25 nm and 65 nm, respectively, which are consistent with the results drawn from the X-ray diffraction study. The particles possess well defined boundaries with lesser agglomeration. TEM images of the lithium incorporated $\text{Gd}_{1.75}\text{Eu}_{0.1}\text{Li}_{0.15}\text{O}_3$ sample shows well connected particles with nearly cobblestone like morphology. Comparing the images of $\text{Gd}_{1.9}\text{Eu}_{0.1}\text{O}_3$ and $\text{Gd}_{1.75}\text{Eu}_{0.1}\text{Li}_{0.15}\text{O}_3$ nanophosphors, the morphology and size of the particles differ significantly indicating the flux effect and change in reaction kinetics, when compensated by lithium ions. The high resolution TEM images show clear lattice fringes indicating superior crystal qualities with nanocrystalline nature and no apparent defects or dislocations. Observed spacing between the adjacent lattice planes is about 0.312 nm, which corresponds to the interplanar spacing between the two (222) crystal planes of cubic structured Gd_2O_3 . SAED patterns of both the samples show continuous dot rings, representing the polycrystalline nature and the indexed SAED patterns are in agreement with the standard JCPDS data of Gd_2O_3 .

3.2 Optical studies

Optical band gap energy (E_g) of the $\text{Gd}_{1.9-x}\text{Eu}_{0.1}\text{Li}_x\text{O}_3$ nanophosphors were determined from the diffuse reflectance spectra employing the Kubelka-Munk method.^{29,30} The expression connecting the diffuse reflectance of the sample (R_∞), absorption coefficient (K) and scattering coefficient (S) is

$$\frac{K}{S} = \frac{(1-R_\infty)^2}{2R_\infty} \equiv F(R_\infty) \quad (2)$$

where $R_\infty = R_{\text{sample}}/R_{\text{reference}}$, is the diffuse reflectance of the sample relative to the BaSO_4 reference at each wavelength, $F(R_\infty)$ is the Kubelka-Munk function. Band gap energy (E_g) of the samples were determined by plotting the variation of Kubelka-Munk function with photon energy according to the relation

$$F(R_{\infty})h\nu \propto (h\nu - E_g)^n \quad (3)$$

Here $h\nu$ is the incident photon energy and the value of the exponent n , which depends on the type of optical transition triggered by photon absorption. Fig. 4 represents the typical Kubelka-Munk plots of $\text{Gd}_{1.9-x}\text{Eu}_{0.1}\text{Li}_x\text{O}_3$ nanophosphors. Band gap energy values were determined by the extrapolation of the linear portion of the $(F(R_{\infty})h\nu)^2$ curve against the photon energy, $h\nu$ to zero. From the figure, it can be seen that the direct band gap of all the lithium incorporated phosphors is higher than that of the non-substituted one. It was found that the band gap of $\text{Gd}_{1.9-x}\text{Eu}_{0.1}\text{Li}_x\text{O}_3$ nanophosphors increases with Li^+ content up to 0.1 and then it remains at 5.73 eV (± 0.01 eV). The band structure and band gap of a compound are determined by the geometrical arrangement and the electronic configurations of the constituting elements. The observed variation in the band gap values of $\text{Gd}_{1.9-x}\text{Eu}_{0.1}\text{Li}_x\text{O}_3$ nanophosphors can be expected to be due to a number of reasons, which include the degree of structural order-disorder in the host lattice by Li^+ incorporation, extend of compressive strain produced in the lattice by the substitution of smaller Li^+ ions in place of larger Gd^{3+} ions, charge imbalance, extend of oxygen vacancies and defects in the lattice. These effects have expected to change the energy level distribution and density of states in the host lattice. Some of the factors cause band gap widening whereas some results in band gap narrowing. Earlier studies have shown that compressive strain in the lattice causes band gap widening whereas oxygen vacancies results in narrowing of band gap.^{18,31} For lower Li^+ content, band gap widening can occur predominantly due to the compressive strain in the lattice. For higher Li^+ content, large number of oxygen vacancies produced in the lattice can cause narrowing of band gap. Both these effects played their complementary roles in higher Li^+ substituted phosphors and as a result band gap remains more or less constant for higher Li^+ compensated phosphors.

Raman spectroscopy is a highly promising spectroscopic tool to investigate the vibrational phonon modes, lattice defects, dislocations, lattice strains, local cation distribution, charge-lattice and spin-lattice couplings of materials.^{32,33} The normalised microRaman spectra of $\text{Gd}_{1.9-x}\text{Eu}_{0.1}\text{Li}_x\text{O}_3$ nanophosphors excited by 785 nm diode laser are presented in Fig. 5(A). The host lattice Gd_2O_3 is cubic structured with space group $\text{Ia}\bar{3}$ (Th^7) and having $Z = 16$. So the expected optical (Γ_{op}) and acoustical (Γ_{ac}) phonon modes by factor group analysis³⁴ are expressed as

$$\Gamma_{\text{op}} = 4A_g + 4E_g + 14F_g + 5A_{2u} + 5E_u + 16F_u, \quad \Gamma_{\text{ac}} = F_u \quad (4)$$

Here A_g is the Raman active symmetric stretching mode, F_g is the Raman active triply degenerate symmetric stretching mode and E_g is the Raman active doubly degenerate symmetric bending mode. A_{2u} and E_u are both Raman and IR inactive and F_u is infrared (IR) active. As a result, 22 Raman vibrational modes of A_g , E_g , and F_g and 16 F_u vibrational IR modes are expected. $Gd_{1.9-x}Eu_{0.1}Li_xO_3$ nanophosphors showed Raman active vibration modes at 97, 120, 137, 146, 316, 362, 445 and 569 cm^{-1} corresponding to cubic Gd_2O_3 and are in accordance with the values reported by Luyer *et al.*³⁵ The intense Raman band located at 362 cm^{-1} is assigned as the combined F_g+A_g vibrational mode having large polarizability change. The phonon modes of materials are determined by the effective mass, bond type and symmetry of the constituting atoms in the primitive unit cell. A careful investigation of the Raman mode located at 362 cm^{-1} indicated a shift to higher wave numbers (361.66 to 362.35 cm^{-1}) with increase in lithium content and is shown in Fig. 5(B). It is expected that lithium incorporation may lead to the shortening of bond lengths, change in force constant and local disorders. The average mass of the nanophosphor decreases with increase in lithium content, which also leads to the shift of phonon modes to higher frequency side.

3.3 Luminescence dynamics, Judd-Ofelt and radiative analysis

Fig. 6 shows the excitation spectra of $Gd_{1.9-x}Eu_{0.1}Li_xO_3$ nanophosphors monitoring the $^5D_0 \rightarrow ^7F_2$ emission at 612 nm of Eu^{3+} . Excitation spectra of the samples consist of an intense high energy broad band with wavelength ranging from 220 to 300 nm and contain several sharp lines. Generally, charge transfer (CT) transitions occur when a valence electron is transferred from the ligand to the unfilled orbitals of the rare earth ion. The observed high energy broad excitation band is assigned as the charge transfer band (CTB), which originates from the transfer of an electron from the filled O^{2-} ($2p^6$) ligand orbital to the 4f orbital of Eu^{3+} .^{1,36} Excitation lines observed at 276, 278 and 280 nm arise from the $^8S_{7/2} \rightarrow ^6I_{7/2-17/2}$ and at 314 nm arise from the $^8S_{7/2} \rightarrow ^6P_{3/2-7/2}$ intra f-f transitions of Gd^{3+} ion from its ground state of $^8S_{7/2}$. These transitions indicate the energy transfer between trivalent gadolinium and europium ions. Excitation lines in the lower energy region occur with lesser intensity compared to CT transition, which results from the intrinsic intra f-f transitions of Eu^{3+} from its ground state 7F_0 to the higher excited states and the observed electronic transitions are assigned as $^7F_0 \rightarrow ^5H_6$ at 323 nm, $^7F_0 \rightarrow ^5D_4$ at 364 nm, $^7F_0 \rightarrow ^5G_{2-6}$ at 383 nm, $^7F_0 \rightarrow ^5L_6$ at 395 nm, $^7F_0 \rightarrow ^5D_3$ at 416 nm, $^7F_0 \rightarrow ^5D_2$ at 467 nm and $^7F_0 \rightarrow ^5D_1$ at 533 nm.⁵ Even though the excitation spectra did not exhibit evident differences in the position and shape of transitions, intensity of the charge transfer band is found enhanced by the monovalent lithium

incorporation. The occurrence of strong charge transfer band is favourable for the effective energy transfer from the host lattice to the activator and hence the luminescence of Eu^{3+} ion.³⁷ This indicate enhanced absorption by the Eu^{3+} ions in presence of Li^+ ions and out of the compositions studied, intensity of the charge transfer band is the highest for $\text{Gd}_{1.75}\text{Eu}_{0.1}\text{Li}_{0.15}\text{O}_3$ phosphor. This makes excitation through the charge transfer band efficient. Position of the CT band in the phosphor is determined by the covalency of O^{2-} and Eu^{3+} , Eu-O bond distance, charge of the ligand and coordination of the central Eu^{3+} ion.^{1,38,39}

The emission from inorganic phosphors originates from the complex interaction among the host matrix, activators, defects, sensitizers and interfaces. Luminescence of the trivalent europium ions results from the intra 4f-4f electron transitions. Since the 4f electrons are well shielded from the surrounding environment by the external electric fields of the outer closed 5s and 5p electrons, characteristic narrow line like emissions are produced. Fig. 7 shows the emission spectra of $\text{Gd}_{1.9-x}\text{Eu}_{0.1}\text{Li}_x\text{O}_3$ nanophosphors under 265 nm charge transfer excitation. The emission spectra indicated no significant change in the position of the peaks, but the relative intensities of transitions changed considerably with lithium incorporation. Each emission spectrum consists of five groups of sharp emission peaks lying between 550 and 720 nm. These narrow and sharp transitions are indexed as the electronic transitions from the excited $^5\text{D}_0$ level to lower $^7\text{F}_J$ ($J = 0, 1, 2, 3$ and 4) manifolds of Eu^{3+} ions and are assigned as the $^5\text{D}_0 \rightarrow ^7\text{F}_0$ (581 nm), $^5\text{D}_0 \rightarrow ^7\text{F}_1$ (588, 593, 599 nm), $^5\text{D}_0 \rightarrow ^7\text{F}_2$ (612, 630 nm), $^5\text{D}_0 \rightarrow ^7\text{F}_3$ (651 nm) and $^5\text{D}_0 \rightarrow ^7\text{F}_4$ (707 nm) transitions.⁵ Of these transitions, the $^5\text{D}_0 \rightarrow ^7\text{F}_2$ transition centred at 612 nm is the dominant one in the emission spectra of all the samples. The emission features of Eu^{3+} activated phosphors strongly depend on the crystal structure of the host and the site occupancy of Eu^{3+} ions in the host matrix.¹ In the body centred cubic Gd_2O_3 crystal structure, Eu^{3+} ions can occupy two crystallographically non-equivalent cationic sites with six-fold coordination viz., a 24d site having C_2 point non-inversion symmetry and 8b site having S_6 point inversion symmetry. The C_2 site lacks inversion centre, whereas the S_6 site is inversion symmetric and the ratio of the probability of occupancy of Eu^{3+} ions in C_2 and S_6 sites is 3:1. The $^5\text{D}_0 \rightarrow ^7\text{F}_2$ transition is symmetry sensitive and parity forbidden forced electric dipole transition with the selection rule $\Delta J=2$, which can be induced by the lattice sites C_2 of Eu^{3+} ions without inversion symmetry and the break of parity selection rules, whereas $^5\text{D}_0 \rightarrow ^7\text{F}_1$ is a structurally independent parity allowed magnetic dipole transition.^{40,41} If more Eu^{3+} ions are occupied in S_6 sites with inversion centre, then the intensity of the pure magnetic dipole transition $^5\text{D}_0 \rightarrow ^7\text{F}_1$ with selection rule $\Delta J=1$ is dominant.

The electric dipole transition of ${}^5D_0 \rightarrow {}^7F_2$ is dominant in the $Gd_{1.9-x}Eu_{0.1}Li_xO_3$ nanophosphors suggesting that Eu^{3+} ions prefer to occupy the low symmetry site without an inversion centre.

The crystal field asymmetry of coordination polyhedron around the Eu^{3+} ions can be determined by evaluating the hypersensitive asymmetric ratio (A). It can also provide an estimate of the covalent nature and polarization of the surrounding of the Eu^{3+} ions by short range effects. Higher the asymmetric ratio, higher is the distortion from inversion symmetry and is evaluated as the ratio of the integrated emission intensity of electric (${}^5D_0 \rightarrow {}^7F_2$) to magnetic (${}^5D_0 \rightarrow {}^7F_1$) dipole transitions^{1,42} as

$$\text{Asymmetric ratio (A)} = \frac{\int I({}^5D_0 - {}^7F_2)}{\int I({}^5D_0 - {}^7F_1)} \quad (5)$$

This ratio depends on the cation site occupancies, bond lengths, bond angles, distortion of the lattice and nature of the host matrix.⁴³ The calculated asymmetric ratio and the integrated emission intensity of the nanophosphors with different Li^+ content are shown in Fig. 8 and the partial energy level diagram illustrating the excitation and emission process in $Gd_{1.9-x}Eu_{0.1}Li_xO_3$ nanophosphors is shown in Fig. 9. Initially, the asymmetric ratio increases with Li^+ content and reaches a value of 5.955 for $Gd_{1.75}Eu_{0.1}Li_{0.15}O_3$, indicating high asymmetric environment of the coordination polyhedron around Eu^{3+} ion and then the value decreases. The observed increase in asymmetric ratio due to Li^+ incorporation indicates reduction in crystal field symmetry around the Eu^{3+} , which in turn increases the probabilities of the various intra 4f-4f transitions of Eu^{3+} ions. It is interesting to note that Li^+ compensation enhances the intensity of photoemission, keeping the shape and position of the electronic transitions unaltered (Fig. 7). It can be seen that the emission intensity first increases with increase of Li^+ content up to 0.15 and then decreases due to the increased rate of non-radiative energy transfer to quenching sites and surface defects. In the present study, the composition $Gd_{1.75}Eu_{0.1}Li_{0.15}O_3$ is found to be highly luminescent and its emission intensity is estimated to be 1.83 times that of $Gd_{1.9}Eu_{0.1}O_3$. There are several factors which may contribute to the improvement of photoluminescence intensity in these phosphors. Sohn *et al.*⁴⁴ reported that lithium incorporation may create a lower symmetry around the rare earth activator ions. In the present study, Li^+ causes reduction in symmetry around Eu^{3+} as reflected in the asymmetric ratios of $Gd_{1.9-x}Eu_{0.1}Li_xO_3$. Besides charge imbalance, the substitution of trivalent gadolinium by monovalent lithium can create oxygen vacancies in the lattice. Oxygen vacancies can act as a sensitizer to promote energy transfer from the host to

the activator, up to a critical defect density¹⁷ and it produces an increase in distortion of the crystal field around the activator. Improved morphology, better crystallinity, larger grains, lesser defects, efficient energy transfer and reduced local crystal field symmetry around Eu^{3+} ions caused more optical activation in presence of Li^+ ions, which lead to increase in emission intensity at lower lithium contents.^{13,17,45} But excess lithium compensation causes oxygen vacancies to increase in the crystal lattice and results in luminescence quenching by energy transfer or migration to the quenching sites.^{1,13,46}

In general, the emission colour of any photoemitter can be represented by the (x, y) chromaticity coordinates in the Commission Internationale de l'Eclairage (CIE) 1931 diagram.⁴⁷ The chromaticity coordinates (x, y) of the phosphors were calculated from the corresponding photoemission spectrum based on the CIE 1931 colour matching functions. Table 1 lists the CIE chromaticity coordinate values of $\text{Gd}_{1.9-x}\text{Eu}_{0.1}\text{Li}_x\text{O}_3$ phosphors and the corresponding 1931 CIE chromaticity diagram for different Li^+ compensated phosphors is shown in Fig. 10. All these values are in the red region of the diagram and no significant change of chromaticity coordinates were observed. Colour purity of a particular dominant colour from a light source is measured as the ratio of the distance between the emission colour coordinates and the coordinates of equal energy point to the distance between the equal energy point and the dominant wavelength point in the CIE diagram.^{48,49} The effect of Li^+ on the colour purity of phosphor is analyzed using

$$\text{Colour purity} = \frac{\sqrt{(x-x_i)^2 + (y-y_i)^2}}{\sqrt{(x_d-x_i)^2 + (y_d-y_i)^2}} \times 100 \% \quad (6)$$

where (x_d, y_d) , (x, y) and (x_i, y_i) are the coordinates of the dominant wavelength, emission light and of the CIE white illuminant E ($x_i = 0.3333$, $y_i = 0.3333$), respectively. Colour purity of all the $\text{Gd}_{1.9-x}\text{Eu}_{0.1}\text{Li}_x\text{O}_3$ phosphors was found to be more than 95 %. Correlated colour temperature (CCT), a measure to characterize the quality of emission from photoemitters is determined by McCamy method⁵⁰ and is expressed as

$$\text{CCT} = 449n^3 + 3525n^2 + 6823.3n + 5520.33 \quad (7)$$

where $n = (x - x_e)/(y_e - y)$ is the inverse slope line and (x_e, y_e) as $(0.3320, 0.1858)$ is the epicentre (Table 1). The CCT values obtained for $\text{Gd}_{1.9-x}\text{Eu}_{0.1}\text{Li}_x\text{O}_3$ phosphor were in the

range, 2052–2130 K and are shown in the correlated colour temperature diagram (Fig. 10(B)).

Transient emission decay curves (Fig. 11) of 612 nm, ${}^5D_0 \rightarrow {}^7F_2$ radiative transition with excitation at 265 nm were used to probe the luminescence dynamics of Eu^{3+} ions in the Li^+ incorporated Gd_2O_3 host matrix. The normalized decay curves observed were fitted using the single exponential method as

$$I(t) = I_0 \exp\left(-\frac{t}{\tau}\right) \quad (8)$$

where $I(t)$ is the emission intensity at time t , I_0 is the initial emission intensity at $t = 0$ s and τ is the lifetime of the emitter. Monoexponential decay behaviour shows the possibility of only one type of emission centre in the phosphor. The lifetime values of $\text{Gd}_{1.9-x}\text{Eu}_{0.1}\text{Li}_x\text{O}_3$ nanophosphors were 1.21716, 1.24565, 1.2771, 1.35888 and 1.2603 ms with Li^+ content of 0, 0.05, 0.1, 0.15 and 0.2, respectively. It is found that the lifetime of the phosphor initially increases with Li^+ content and then decreases due to increase in non-radiative energy transfer by energy migration to quenching sites. Consequently, shortening of lifetime and decrease of emission intensity was observed.

Detailed investigation on the site symmetry and luminescence dynamics of Eu^{3+} ions in $\text{Gd}_{1.9-x}\text{Eu}_{0.1}\text{Li}_x\text{O}_3$ was evaluated by analysing the Judd-Ofelt intensity parameters. Judd-Ofelt analysis^{51,52} is a powerful spectroscopic technique, which effectively describes the spectral behaviour in a specific coordination environment of rare earth ion doped single and polycrystalline materials, glasses and solutions. Through this analysis one can determine the rates of parity forbidden electric dipole transitions between different electronic levels of the rare earth ion, understand the local structural environment around the rare earth ion and can evaluate the bond covalency of rare earth and its associated ligands. The three Judd-Ofelt (J-O) intensity parameters, Ω_λ ($\lambda = 2, 4$ and 6) can act as a probe to identify the structural environment and symmetry of rare earth ions in host matrices. Detailed physical interpretation of these parameters was discussed by Jorgensen and Reisfeld.⁵³ These parameters were determined from the photoemission spectrum considering the intensity of 5D_0 - 7F_1 magnetic dipole allowed transition as the reference, since it is unaltered by the surrounding crystal field environment. Judd-Ofelt theory gives the spontaneous emission probability of 5D_0 - 7F_1 magnetic dipole transition (A_{01}) as

$$A_{01} = \frac{64\pi^4 \nu_1^3 n^3 S_{md}}{3h(2J+1)} \quad (9)$$

The electric dipole transition rates (A_{0J}) of ${}^5D_0 \rightarrow {}^7F_J$ ($J = 2, 4$ and 6) transitions are given by

$$A_{0J} = \frac{64\pi^4 \nu_J^3}{3h(2J+1)} e^2 \frac{n(n^2+2)^2}{9} \sum_{\lambda=2,4,6} \Omega_\lambda \left| \langle {}^5D_0 \| U^{(\lambda)} \| {}^7F_J \rangle \right|^2 \quad (10)$$

Here 'e' is the electron charge, ν_J is wavenumber of the respective electronic transition, $(2J+1)$ equals 1 for 5D_0 transitions, h is the Planck's constant, S_{md} is the magnetic dipolar line strength of the ${}^5D_0 \rightarrow {}^7F_1$ transition, which is independent of the host matrix, equal to 9.6×10^{-42} units and 'n' is the effective refractive index of the nanophosphor.^{54,55} Effective refractive index (n) of the nanophosphors was determined using the equation⁵⁵

$$n = xn_b + (1-x)n_m \quad (11)$$

where n_b is the refractive index of the bulk ($n_b=1.935$), n_m is the refractive index of the surrounding medium ($n_m=1$ for air) and 'x' is the optical filling factor. The filling factor represents the fraction of the space occupied by the nanophosphor. The emission lifetimes of the 5D_0 state in bulk ($\tau_b=0.94$ ms) and nanocrystals (τ_s) are related to the refractive index of the bulk (n_b) and refractive index of the sample (n_s) by

$$\frac{\tau_b}{\tau_s} (n_b^2 + 2)^2 n_b = n_s^5 + 4n_s^3 + 4n_s \quad (12)$$

Solving this equation, the optical filling factor 'x' can be determined as

$$x = \frac{n_s - n_m}{n_b - n_m} \quad (13)$$

The squared reduced matrix element $\left| \langle {}^5D_0 \| U^{(\lambda)} \| {}^7F_J \rangle \right|^2$ is independent of the surrounding environment of the Eu^{3+} ion and the values are 0.00324, 0.00229 and 0.00023 for $J = 2, 4$ and 6 , respectively.⁶ Because of the selection rules and the unique nature of transition intensities of Eu^{3+} ions, each of the $\left| \langle {}^5D_0 \| U^{(\lambda)} \| {}^7F_J \rangle \right|^2$ values determine the intensities of the corresponding transitions since the other two reduced matrix elements are zero. As a result the Judd-Ofelt intensity parameters can be determined from the ratio of the intensities of electric to magnetic dipole transitions given by

$$\frac{\int I_J d\nu}{\int I_1 d\nu} = \frac{A_{0J}}{A_{01}} = \frac{e^2 \nu_J^3 (n^2+2)^2}{S_{md} \nu_1^3 9n^2} \Omega_\lambda \left| \langle {}^5D_0 \| U^{(\lambda)} \| {}^7F_J \rangle \right|^2 \quad (14)$$

Table 2 summarizes the Judd-Ofelt intensity parameters and emission intensity ratios

of the major electronic transitions from the 5D_0 level of Eu^{3+} to 7F_J manifolds in $\text{Gd}_{1.9-x}\text{Eu}_{0.1}\text{Li}_x\text{O}_3$ nanophosphors. The Judd-Ofelt intensity (J-O) parameters are important for investigating the local structure, local crystal symmetry and bonding in the vicinity of rare earth ions.^{56,57} Wang *et al.*⁵⁸ suggested the dependence of Ω_2 parameter on the covalence of rare earth ions with coordinating ligands and the site symmetry of the local environment of Eu^{3+} ion. Jiang *et al.*⁵⁹ pointed out that if higher is the asymmetry around Eu^{3+} ion, higher will be the Ω_2 parameter. This means that Ω_2 parameter value is attributed to the covalency and structural changes in the vicinity of the Eu^{3+} ion exhibiting short range effect whereas the Ω_4 parameter is dependent on the viscosity and dielectric constant of the host causing long range effect.⁶⁰ Large values for Ω_4 represent low rigidity of the host matrices. The Ω_6 intensity parameter could not be calculated here because 5D_0 - 7F_6 emission located in the infrared region was quite weak and was not observed in the present case. For $\text{Gd}_{1.9-x}\text{Eu}_{0.1}\text{Li}_x\text{O}_3$ nanophosphor, the Ω_2 value is increased with the increase of Li^+ content up to 0.15, which indicates stronger covalence of Eu-O bonding and lower symmetry around the Eu^{3+} ion. Low symmetry is suitable for the enhanced emission of Eu^{3+} ions at 612 nm because the 5D_0 - 7F_2 electric dipole transition is highly sensitive to its local environment. Smaller values of Ω_4 obtained shows appreciable rigidity of the crystalline host matrix. Electronic transitions from the 5D_0 level to low-lying 7F_J manifolds with $J=0, 3$ or 5 are electrically and magnetically forbidden by Judd-Ofelt theory, since their correlated reduced matrix elements are zero.^{51,52} Possible reason for the observed weak emission transitions to these levels is attributed to the crystal field induced J-mixing, which borrows intensity from the allowed electric dipole transitions by the even crystal field interaction.⁶ The extent of this J-mixing was evaluated using the R_{02} ratio given in table 2 and the Judd-Ofelt intensity parameters were also determined by considering this J-mixing effect (see Table 2). The tendency of the J-O parameters in all the lithium compensated $\text{Gd}_{1.9-x}\text{Eu}_{0.1}\text{Li}_x\text{O}_3$ nanophosphor is found to be in the order $\Omega_2 > \Omega_4$.

Radiative parameters such as radiative transition probability, radiative lifetime, quantum efficiency, branching ratios and stimulated emission cross-sections for 5D_0 - 7F_J transitions of Eu^{3+} ions in $\text{Gd}_{1.9-x}\text{Eu}_{0.1}\text{Li}_x\text{O}_3$ phosphor were determined from their emission spectra. The total radiative transition probability (A_R) is obtained by summing over all the radiative rates A_{0J} for each 5D_0 - 7F_J transition and is expressed as

$$A_R = \sum_J A_{0J} = A_{01} \frac{\nu_{01}}{I_{01}} \sum_{J=0}^4 \frac{I_{0J}}{\nu_{0J}} \quad (15)$$

where ν_{01} and ν_{0J} are the energy barycentre of the ${}^5D_0-{}^7F_1$ and ${}^5D_0-{}^7F_J$ transitions, A_{01} is the Einstein's coefficient between ${}^5D_0-{}^7F_1$ levels, I_{0J} is the integrated area of the emission spectrum corresponding to the particular ${}^5D_0-{}^7F_J$ transition.

The radiative lifetime (τ_{rad}) of the excited 5D_0 level is the reciprocal of the total radiative transition rate and is expressed as

$$\tau_{\text{rad}} = \frac{1}{\sum_J A_{0J}} = \frac{1}{A_R} \quad (16)$$

The luminescence lifetime (τ_{obs}) of the Eu^{3+} first excited state, 5D_0 was measured at 612 nm with an excitation wavelength of 265 nm. This lifetime (τ_{obs}) of 5D_0 state is determined by the radiative, A_R and non-radiative, A_{NR} transition rates, which is closely related to the crystalline environment around the Eu^{3+} ions and is given by

$$\frac{1}{\tau_{\text{obs}}} = A_T = A_R + A_{\text{NR}} \quad (17)$$

where A_T is the total transition rate. The luminescence quantum efficiency (η) is the ratio of the number of photons emitted to the number of photons absorbed by the Eu^{3+} luminescent centres. Using the emission spectra and lifetime of the 5D_0 emission level, the quantum efficiency of the Eu^{3+} ion excited state can be determined. Assuming that non-radiative and radiative processes are involved in the depopulation of the 5D_0 state, η can be determined by

$$\eta = \frac{\tau_{\text{obs}}}{\tau_{\text{rad}}} = \frac{A_R}{A_R + A_{\text{NR}}} = \tau_{\text{obs}} A_R \quad (18)$$

The relative intensity of a particular emission transition with respect to all other transitions from an excited electronic state is measured as the fluorescence branching ratio and this ratio (β_{0J}) for the emission from the 5D_0 level to a low lying level 'J' of Eu^{3+} is expressed as

$$\beta_{0J} = \frac{A_{0J}}{\sum A_{0J}} \quad (19)$$

Judd-Ofelt theory can also be used to evaluate the induced emission cross-sections of electronic transitions. The peak stimulated emission cross-sections have been calculated from the emission spectra by Fuchtbabauer-Landenburg formula⁶¹ and is related to the radiative transition rate (A_{0J}) as

$$\sigma_{0J} = \frac{\lambda_p^4}{8\pi c n^2 \Delta\lambda_{\text{eff}}} A_{0J} \quad (20)$$

where λ_p is the peak wavelength of emission band and $\Delta\lambda_{\text{eff}}$ is the effective line width of the emission transition.

Transition rates (A_R , A_{NR} and A_T), lifetime (τ_{rad} and τ_{obs}), quantum efficiency (η), branching ratios (β_{00} , β_{01} , β_{02} , β_{03} and β_{04}) and emission cross-sections (σ_{01} , σ_{02} and σ_{04}) of $\text{Gd}_{1.9-x}\text{Eu}_{0.1}\text{Li}_x\text{O}_3$ nanophosphors are summarized in table 3. The branching ratios of emission transitions follow the trend as $\beta_{02} > \beta_{01} > \beta_{04} > \beta_{03} > \beta_{00}$ and emission cross sections follow the trend as $\sigma_{02} > \sigma_{01} > \sigma_{04}$ in all the samples. A comparison of the luminescence properties obtained in the present study with other reports available in the literature is presented in Table 4. Variation of lifetime and quantum efficiency of $\text{Gd}_{1.9-x}\text{Eu}_{0.1}\text{Li}_x\text{O}_3$ nanophosphors with Li^+ content is depicted in Fig. 12. With Li^+ content, quantum efficiency and lifetime values increase and the highest quantum efficiency of 83.93 % with a lifetime of 1.35888 ms is obtained for the $\text{Gd}_{1.75}\text{Eu}_{0.1}\text{Li}_{0.15}\text{O}_3$ nanophosphor. Thereafter quantum efficiency and lifetime values decrease due to the increased rate of non-radiative relaxations. Clearly, the incorporation of Li^+ ions reduces the non-radiative relaxation and increases the quantum efficiency of $\text{Gd}_{1.9}\text{Eu}_{0.1}\text{O}_3$ phosphors.

4. Conclusions

Highly luminescent $\text{Gd}_2\text{O}_3:\text{Eu}^{3+}$, Li^+ nanophosphors were successfully synthesized by the controlled solvothermal combustion in diethylene glycol medium. It is found that lithium compensation promotes grain growth resulting in better crystallization. Morphology of the $\text{Gd}_{1.9-x}\text{Eu}_{0.1}\text{Li}_x\text{O}_3$ nanophosphors is found to be highly sensitive to the extent of compensation by the lithium ions. All the lithium compensated phosphors showed enhanced $^5\text{D}_0$ - $^7\text{F}_J$ ($J = 1-4$) photoemissions of Eu^{3+} under charge transfer excitation. The improvement of emission intensity and quantum efficiency is attributed to the improved crystallinity and grain size leading to higher oscillator strengths for the 4f-4f electronic transitions and reduction of symmetry around the Eu^{3+} with lithium ion compensation. The highest emission intensity was observed for $\text{Gd}_{1.75}\text{Eu}_{0.1}\text{Li}_{0.15}\text{O}_3$ composition and was found to be 1.83 times that of $\text{Gd}_{1.9}\text{Eu}_{0.1}\text{O}_3$ phosphor. The luminescence decay profiles follow single exponential kinetics. Higher value of Judd-Ofelt intensity parameters indicate highly polarized local environment, higher covalency and more asymmetry around the europium ions. Strong visible emissions, large stimulated emission cross-sections, better quantum efficiency and higher branching ratio make these nanophosphors as a novel luminescent material. The present report highlights the use of monovalent lithium compensation as a strategy to enhance the emission features of rare earth activated nanophosphors.

Acknowledgement

R. G. Abhilash Kumar acknowledges University Grants Commission (UGC), India for the award of teacher fellowship under the Faculty Development Programme.

References

- 1 G. Blasse and B. C. Grabmaier, *Luminescent Materials*, Springer-Verlag, Berlin, 1994.
- 2 Y. Liu, D. Tu, H. Zhu, R. Li, W. Luo and X. Chen, *Adv. Mater.*, 2010, **22**, 3266.
- 3 L. Liu, E. Ma, R. Li, G. Liu and X. Chen, *Nanotechnology*, 2007, **18**, 015403.
- 4 A. G. Macedo, R. A. S. Ferreira, D. Ananias, M. S. Reis, V. S. Amaral, L. D. Carlos and J. Rocha, *Adv. Funct. Mater.*, 2010, **20**, 624.
- 5 J. Yang, C. X. Li, Z. Y. Cheng, X. M. Zhang, Z. W. Quan, C. M. Zhang and J. Lin, *J. Phys. Chem. C*, 2007, **111**, 18148.
- 6 L. Liu and X. Chen, *Nanotechnology*, 2007, **18**, 255704.
- 7 H. Guo, N. Dong, M. Yin, W. Zhang, L. Lou and S. Xia, *J. Phys. Chem. B*, 2004, **108**, 19205.
- 8 G. Jia, K. Liu, Y. H. Zheng, Y. H. Song, M. Yang and H. P. You, *J. Phys. Chem. C*, 2009, **113**, 6050.
- 9 M. Nichkova, D. Dosev, S. J. Gee, B. D. Hammock and I. M. Kennedy, *Anal. Chem.*, 2005, **77**, 6864.
- 10 M. Nichkova, D. Dosev, R. Perron, S. J. Gee, B. D. Hammock and I. M. Kennedy, *Anal. Bioanal. Chem.*, 2006, **384**, 631.
- 11 M. Ahren, L. Selegard, A. Klasson, F. Soderlind, N. Abrikossova, C. Skoglund, T. Bengtsson, M. Engstrom, P. Kall and K. Uvdal, *Langmuir*, 2010, **26**, 5753.
- 12 R. Balakrishnaiah, S. S. Yi, K. Jang, H. S. Lee, B. K. Moon and J. H. Jeong, *Mater. Res. Bull.*, 2011, **46**, 621.
- 13 J. Y. Cho, Y. R. Do and Y. D. Huh, *Appl. Phys. Lett.*, 2006, **89**, 131915.
- 14 J. H. Jeong, J. S. Bae, S. S. Yi, J. C. Park and Y. S. Kim, *J. Phys.: Condens. Matter*, 2003, **15**, 567.
- 15 L. Sun, C. Quian, C. Liao, X. Wang and C. Yan, *Solid State Commun.*, 2001, **119**, 393.
- 16 S. S. Yi, J. S. Bae, K. S. Shim, J. H. Jeong, J. C. Park and P. H. Holloway, *Appl. Phys. Lett.*, 2004, **84**, 353.
- 17 J. C. Park, H. K. Moon, D. K. Kim, S. H. Byeon, B. C. Kim and K. S. Suh, *Appl. Phys. Lett.*, 2000, **77**, 2162.

- 18 N. Dhananjaya, H. Nagabhushana, B. M. Nagabhushana, B. Rudraswamy, C. Shivakumara and R. P. S. Chakradhar, *J. Alloys Compd.*, 2011, **509**, 2368.
- 19 N. Dhananjaya, H. Nagabhushana, B. M. Nagabhushana, B. Rudraswamy, C. Shivakumara, K. Narahari and R. P. S. Chakradhar, *Spectrochim Acta A Mol Biomol Spectrosc.*, 2012, **86**, 8.
- 20 J. S. Bae, S. S. Park, T. E. Hong, J. P. Kim, J. H. Yoon, E. D. Jeong, M. S. Won and J. H. Jeong, *Curr. Appl. Phys.*, 2009, **9**, S241.
- 21 H. K. Yang, H. Choi, B. K. Moon, B. C. Choi, J. H. Jeong, J. H. Kim and K. H. Kim, *Solid State Sci.*, 2010, **12**, 1445.
- 22 Q. Ma, Y. Zhou, A. Zhang, M. Lu, G. Zhou and C. Li, *Solid State Sci.*, 2009, **11**, 1124.
- 23 K. A. Hyeon, S. H. Byeon, J. C. Park, D. K. Kim and K. S. Suh, *Solid State Commun.*, 2000, **115**, 99.
- 24 Y. Wu, Y. Nien, Y. Wang and I. Chen, *J. Am. Ceram. Soc.*, 2012, **95**, 1360.
- 25 Z. Xia and D. Chen, *J. Am. Ceram. Soc.*, 2010, **93**, 1397.
- 26 R. G. Abhilash Kumar, Satoshi Hata and K. G. Gopchandran, *Ceram. Int.*, 2013, **39**, 9125.
- 27 R. G. Abhilash Kumar, Satoshi Hata, Ken-ichi Ikeda and K. G. Gopchandran, *Ceram. Int.*, 2015, **41**, 6037.
- 28 S. N. Sarangi and S. N. Sahu, *Int. J. Nanosci.*, 2006, **5**, 109.
- 29 P. Kubelka, *J. Opt. Soc. Am.*, 1948, **38**, 448.
- 30 A. E. Morales, E. S. Mora and U. Pal, *Rev. Mex. Fis.*, 2007, **S53(5)**, 18.
- 31 J. Wang, Z. Wang, B. Huang, Y. Ma, Y. Liu, X. Qin, X. Zhang and Y. Dai, *ACS Appl. Mater. Interfaces*, 2012, **4**, 4024.
- 32 V. Dediu, C. Ferdeghini, F. C. Maticotta, P. Nozar and G. Ruani, *Phys. Rev. Lett.*, 2000, **84**, 4489.
- 33 D. L. Rousseau, R. P. Bauman and S. P. S. Porto, *J. Raman Spectrosc.*, 1981, **10**, 253.
- 34 W. B. White and V. G. Keramidas, *Spectrochim. Acta A*, 1972, **28**, 501.
- 35 C. L. Luyer, A. Garcia-Murillo, E. Bernstein and J. Mugnier, *J. Raman Spectrosc.*, 2003, **34**, 234.
- 36 B. Yan and H. Huang, *Colloids Surf. A*, 2006, **287**, 158.
- 37 M. L. Pang, W. Y. Shen and J. Lin, *J. Appl. Phys.*, 2005, **97**, 033511.
- 38 L. Li and S. Y. Zhang, *J. Phys. Chem. B*, 2006, **110**, 21438.
- 39 L. Li, H. K. Yang, B. K. Moon, B. C. Choi, J. H. Jeong and K. H. Kim, *Mater. Chem. Phys.*, 2010, **119**, 471.

- 40 J. Dhanaraj, R. Jagannathan, T. R. N. Kutty and C. H. Lu, *J. Phys. Chem. B*, 2001, **105**, 11098.
- 41 J. G. Li, X. H. Wang, K. Watanabe and T. Ishigaki, *J. Phys. Chem. B*, 2006, **110**, 1121.
- 42 R. K. Brow, D. R. Tallant and G. L. Turner, *J. Am. Ceram. Soc.*, 1996, **79**, 2410.
- 43 B. Antic, J. Rogan, A. Kremenovic, A. S. Nikolic, M. Vucinic-Vasic, D. K. Bozanic, G. F. Goya and Ph. Colomban, *Nanotechnology*, 2010, **21**, 245702.
- 44 S. H. Sohn, D. G. Hyun, A. Yamada and Y. Hamakawa, *Appl. Phys. Lett.*, 1993, **62**, 991.
- 45 A. K. Singh, S. K. Singh and S. B. Rai, *RSC Adv.*, 2014, **4**, 27039.
- 46 X. Liu, X. Xu, M. Gu, L. Xiao, K. Han and R. Zhang, *Appl. Surf. Sci.*, 2007, **253**, 4344.
- 47 R. W. G. Hunt, *Measuring Colour: Applied Science and Industrial Technology*, Ellis Horwood, New York, 1991.
- 48 G. R. Dillip, K. Mallikarjuna, S. J. Dhoble and B. Deva Prasad Raju, *J. Phys. Chem. Solids*, 2014, **75**, 8.
- 49 Y. C. Fang, S. Y. Chu, P. C. Kao, Y. M. Chuang and Z. L. Zeng, *J. Electrochem. Soc.*, 2011, **158**, J1.
- 50 C. S. McCamy, *Color Research & Application*, 1992, **17**, 142.
- 51 B. R. Judd, *Phys. Rev.*, 1962, **127**, 750.
- 52 G. S. Ofelt, *J. Chem. Phys.*, 1962, **37**, 511.
- 53 C. K. Jorgensen and R. Reisfeld, *J. Less-Common Met.*, 1983, **93**, 107.
- 54 M. J. Weber, T. E. Varitimos and B. H. Matsinger, *Phys. Rev. B*, 1973, **8**, 47.
- 55 R. M. Krsmanovic, Z. Antic, M. G. Nikolic, M. Mitric and M. D. Dramicanin, *Ceram. Int.*, 2011, **37**, 525.
- 56 H. Lin, D. Yang, G. Liu, T. Ma, B. Zhai, Q. An, J. Yu, X. Wang, X. Liu and E. Y. B. Pun, *J. Lumin.*, 2005, **113**, 121.
- 57 R. Saraf, C. Shivakumara, S. Behera, N. Dhananjaya and H. Nagabhushana, *RSC Adv.*, 2015, **5**, 9241.
- 58 J. Wang, H. Song, X. Kong, H. Peng, B. Sun, B. Chen, J. Zhang and W. Xu, *J. Appl. Phys.*, 2003, **93**, 1482.
- 59 Z. Jiang, Y. Jianhu and D. Shixun, *J. Opt. Soc. Am. B*, 2004, **21**, 739.
- 60 W. F. Krupke, *Phys. Rev.*, 1966, **145**, 325.
- 61 M. J. F. Digonnet, *Rare earth doped fiber and amplifiers*, Marcel Dekker, New York, 1993.
- 62 C. Liu, J. Liu and K. Dou, *J. Phys. Chem. B*, 2006, **110**, 20277.

Figure captions

- Fig 1.** X-ray diffraction patterns of $\text{Gd}_{1.9-x}\text{Eu}_{0.1}\text{Li}_x\text{O}_3$ nanophosphors as a function of Li^+ content (x): (a) 0, (b) 0.05, (c) 0.1, (d) 0.15 and (e) 0.2.
- Fig 2.** Variation of lattice constant and cell volume of $\text{Gd}_{1.9-x}\text{Eu}_{0.1}\text{Li}_x\text{O}_3$ nanophosphors as a function of lithium content [Inset: crystallite size]
- Fig 3.** Low and high resolution TEM images and selected area electron diffraction patterns of (a-c) $\text{Gd}_{1.9}\text{Eu}_{0.1}\text{O}_3$ and (d-f) $\text{Gd}_{1.75}\text{Eu}_{0.1}\text{Li}_{0.15}\text{O}_3$ nanophosphors, respectively.
- Fig 4.** Kubelka-Munk plots of $\text{Gd}_{1.9-x}\text{Eu}_{0.1}\text{Li}_x\text{O}_3$ nanophosphors with different Li^+ content (x): (a) 0, (b) 0.05, (c) 0.1, (d) 0.15 and (e) 0.2.
- Fig 5.** Normalised microRaman spectra of $\text{Gd}_{1.9-x}\text{Eu}_{0.1}\text{Li}_x\text{O}_3$ nanophosphors with different lithium content (x): (A)- (a) 0, (b) 0.05, (c) 0.1, (d) 0.15 and (e) 0.2 and (B) Magnified Raman spectrum in the neighbourhood of the peak at 362 cm^{-1} .
- Fig 6.** Excitation spectra of $\text{Gd}_{1.9-x}\text{Eu}_{0.1}\text{Li}_x\text{O}_3$ nanophosphors ($\lambda_{\text{em}}=612\text{ nm}$) with different Li^+ content (x): (a) 0, (b) 0.05, (c) 0.1, (d) 0.15 and (e) 0.2.
- Fig 7.** Emission spectra of $\text{Gd}_{1.9-x}\text{Eu}_{0.1}\text{Li}_x\text{O}_3$ nanophosphors ($\lambda_{\text{ex}}=265\text{ nm}$) with different Li^+ content (x): (a) 0, (b) 0.05, (c) 0.1, (d) 0.15 and (e) 0.2.
- Fig 8.** Variation of integrated emission intensity and asymmetric ratio of $\text{Gd}_{1.9-x}\text{Eu}_{0.1}\text{Li}_x\text{O}_3$ nanophosphors as a function of Li^+ content.
- Fig 9.** Schematic model of partial energy level diagram illustrating the excitation and emission process in $\text{Gd}_{1.9-x}\text{Eu}_{0.1}\text{Li}_x\text{O}_3$ nanophosphors.
- Fig 10.** (A) CIE chromaticity diagram and (B) correlated colour temperature diagram of $\text{Gd}_{1.9-x}\text{Eu}_{0.1}\text{Li}_x\text{O}_3$ nanophosphors with different Li^+ content (x): (a) 0, (b) 0.05, (c) 0.1, (d) 0.15 and (e) 0.2.
- Fig 11.** Luminescence decay curves of Eu^{3+} (${}^5\text{D}_0 \rightarrow {}^7\text{F}_2$ transition at 612 nm , $\lambda_{\text{ex}}=265\text{ nm}$) in $\text{Gd}_{1.9-x}\text{Eu}_{0.1}\text{Li}_x\text{O}_3$ with different Li^+ content (x): (a) 0, (b) 0.05, (c) 0.1, (d) 0.15 and (e) 0.2 (experimental data (o) and fitting results (-)).
- Fig 12.** Variation of lifetime and quantum efficiency of $\text{Gd}_{1.9-x}\text{Eu}_{0.1}\text{Li}_x\text{O}_3$ nanophosphors as a function of Li^+ content.

Table 1. Values of the CIE chromaticity coordinates (x , y), correlated colour temperature (CCT) and colour purity of $\text{Gd}_{1.9-x}\text{Eu}_{0.1}\text{Li}_x\text{O}_3$ nanophosphors.

Li content	Chromaticity coordinates		CCT (K)	Colour purity (%)
	x	y		
0	0.6341	0.3530	2052	95.57
0.05	0.6351	0.3505	2103	95.72
0.10	0.6357	0.3497	2123	95.78
0.15	0.6361	0.3496	2129	95.91
0.20	0.6354	0.3492	2130	95.57

Table 2. Judd-Ofelt intensity parameters (Ω_2 and Ω_4) and ratio of integrated emission intensities of the $^5\text{D}_0 - ^7\text{F}_0$ and $^5\text{D}_0 - ^7\text{F}_2$ (R_{02}), $^5\text{D}_0 - ^7\text{F}_2$ and $^5\text{D}_0 - ^7\text{F}_1$ (R_{21}), $^5\text{D}_0 - ^7\text{F}_4$ and $^5\text{D}_0 - ^7\text{F}_1$ (R_{41}) transitions of $\text{Gd}_{1.9-x}\text{Eu}_{0.1}\text{Li}_x\text{O}_3$ nanophosphors.

$\text{Gd}_{1.9-x}\text{Eu}_{0.1}\text{Li}_x\text{O}_3$	Refractive index	without J mixing		with J mixing		Intensity Ratio		
		Ω_2 ($\times 10^{-20} \text{ cm}^2$)	Ω_4 ($\times 10^{-20} \text{ cm}^2$)	Ω_2 ($\times 10^{-20} \text{ cm}^2$)	Ω_4 ($\times 10^{-20} \text{ cm}^2$)	R_{02}	R_{21}	R_{41}
$\text{Gd}_{1.9}\text{Eu}_{0.1}\text{O}_3$	1.7988	8.514	1.278	9.852	1.427	0.032	5.669	0.390
$\text{Gd}_{1.85}\text{Eu}_{0.1}\text{Li}_{0.05}\text{O}_3$	1.7868	8.751	1.175	10.126	1.313	0.036	5.809	0.358
$\text{Gd}_{1.8}\text{Eu}_{0.1}\text{Li}_{0.1}\text{O}_3$	1.7740	8.837	1.246	10.226	1.392	0.036	5.847	0.378
$\text{Gd}_{1.75}\text{Eu}_{0.1}\text{Li}_{0.15}\text{O}_3$	1.7421	9.071	1.309	10.496	1.462	0.039	5.955	0.394
$\text{Gd}_{1.7}\text{Eu}_{0.1}\text{Li}_{0.20}\text{O}_3$	1.7808	8.294	1.081	9.597	1.207	0.036	5.497	0.328

Table 3. Radiative parameters such as transition rates (A_R , A_{NR} and A_T), lifetimes (τ_{rad} and τ_{obs}), quantum efficiency (η), branching ratios (β_{00} , β_{01} , β_{02} , β_{03} and β_{04}) and stimulated emission cross-sections (σ_{01} , σ_{02} and σ_{04}) of $Gd_{1.9-x}Eu_{0.1}Li_xO_3$ nanophosphors.

Radiative parameter	$Gd_{1.9}Eu_{0.1}O_3$	$Gd_{1.85}Eu_{0.1}Li_{0.05}O_3$	$Gd_{1.8}Eu_{0.1}Li_{0.1}O_3$	$Gd_{1.75}Eu_{0.1}Li_{0.15}O_3$	$Gd_{1.7}Eu_{0.1}Li_{0.20}O_3$
$A_R (s^{-1})$	646.01	648.10	639.59	617.67	608.85
$A_{NR} (s^{-1})$	175.57	154.69	143.43	118.23	184.61
$A_T (s^{-1})$	821.58	802.79	783.02	735.90	793.46
$\tau_{rad} (ms)$	1.54796	1.54297	1.56350	1.61899	1.64243
$\tau_{obs} (ms)$	1.21716	1.24565	1.2771	1.35888	1.26030
$\eta (\%)$	78.63	80.73	81.68	83.93	76.73
$\beta_{00} (\%)$	2.336	2.636	2.618	2.695	2.612
$\beta_{01} (\%)$	13.008	12.709	12.603	12.359	13.392
$\beta_{02} (\%)$	76.113	76.187	76.053	76.158	75.980
$\beta_{03} (\%)$	2.495	3.048	3.045	2.984	2.773
$\beta_{04} (\%)$	6.048	5.420	5.681	5.804	5.243
σ_{01} ($\times 10^{-22} \text{ cm}^2$)	7.4297	7.3982	7.4107	7.5036	7.4222
σ_{02} ($\times 10^{-21} \text{ cm}^2$)	3.9801	4.7680	4.8833	4.9313	4.6002
σ_{04} ($\times 10^{-22} \text{ cm}^2$)	5.9459	5.7931	5.7455	5.9747	4.8699

Table 4. Comparison of the luminescence properties of $\text{Gd}_2\text{O}_3:\text{Eu}^{3+}$ based nanophosphors obtained in this work with other reports. (Bg-Band gap, λ_{ex} -excitation wavelength, λ_{em} -dominant emission wavelength, τ -measured lifetime, η -quantum efficiency)

Composition	Synthesis method	Crystal structure	Morphology	Bg (eV)	λ_{ex} (nm)	λ_{em} (nm)	τ (ms)	η (%)	Judd-Ofelt parameter ($\times 10^{-20} \text{ cm}^2$)		Intensity	Ref.
									Ω_2	Ω_4		
$\text{Gd}_{1.9}\text{Eu}_{0.1}\text{O}_3$	Solution combustion	Cubic	Nanoparticles	5.67	265	612	1.217	78.63	9.85	1.43	-----	27
$\text{Gd}_{1.8}\text{Eu}_{0.2}\text{O}_3$	Solution combustion	Cubic	Microparticles	-----	355	611	1.41	23.6	5.28	1.66	-----	62
$\text{Gd}_2\text{O}_3:\text{Eu}$ (5 mol%)	Hydrothermal method	Cubic	Nanoparticles and nanorods	-----	258	611	2.3	-----	12.39	2.02	-----	6
$\text{Gd}_2\text{O}_3:\text{Eu}$ (4 mol%), Li^+ (6 mol%)	Solution combustion	Monoclinic and cubic	Nanoparticles	5.16	254	612	-----	-----	-----	-----	4 times that of $\text{Gd}_2\text{O}_3:\text{Eu}$ (4 mol %)	18
$\text{Gd}_2\text{O}_3:\text{Eu}^{3+}$ (4 mol%), Li^+ (1 mol%)	Solution combustion	Monoclinic and cubic	Nanoparticles	5.49	243	612	-----	-----	-----	-----	1.64 times that of $\text{Gd}_2\text{O}_3:\text{Eu}^{3+}$ (4 mol%)	19
$\text{Gd}_{1.75}\text{Eu}_{0.1}\text{Li}_{0.15}\text{O}_3$	Solution combustion	Cubic	Nanoparticles	5.73	265	612	1.359	83.93	10.50	1.46	1.83 times that of $\text{Gd}_{1.9}\text{Eu}_{0.1}\text{O}_3$	This work

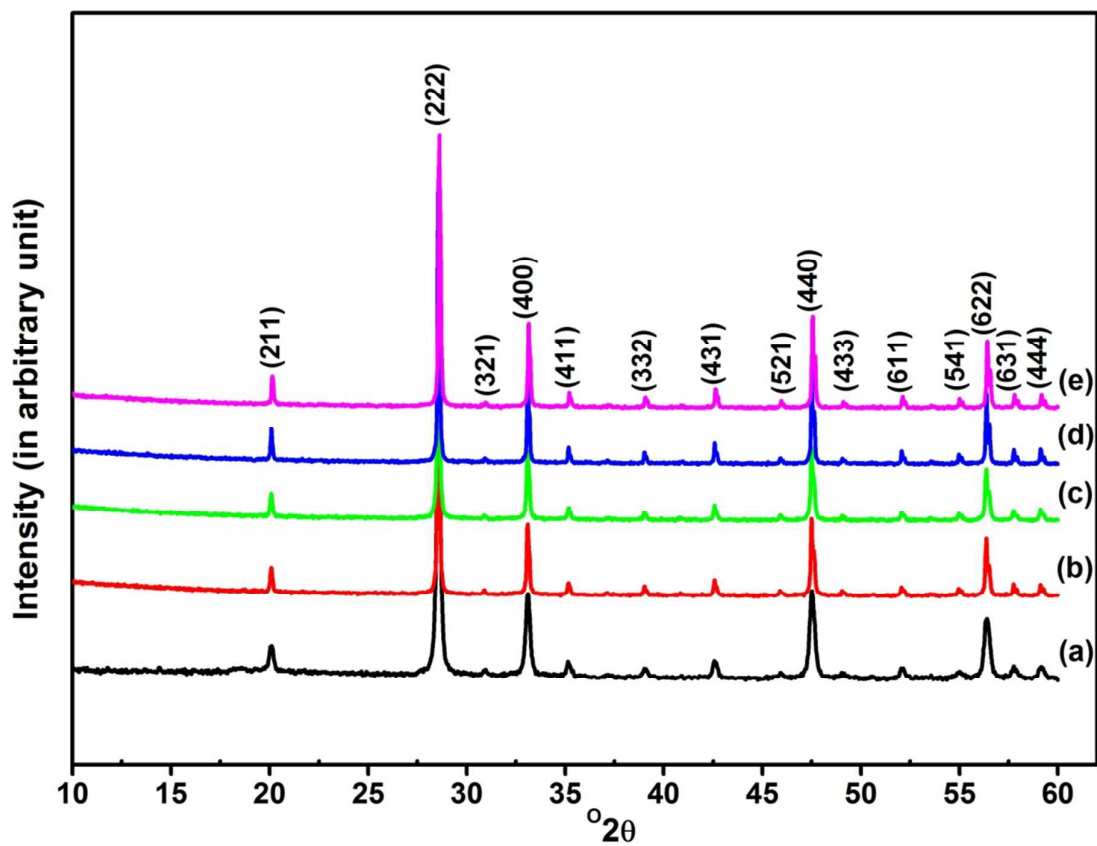


Fig 1. X-ray diffraction patterns of $\text{Gd}_{1.9-x}\text{Eu}_{0.1}\text{Li}_x\text{O}_3$ nanophosphors as a function of Li^+ content (x): (a) 0, (b) 0.05, (c) 0.1, (d) 0.15 and (e) 0.2.

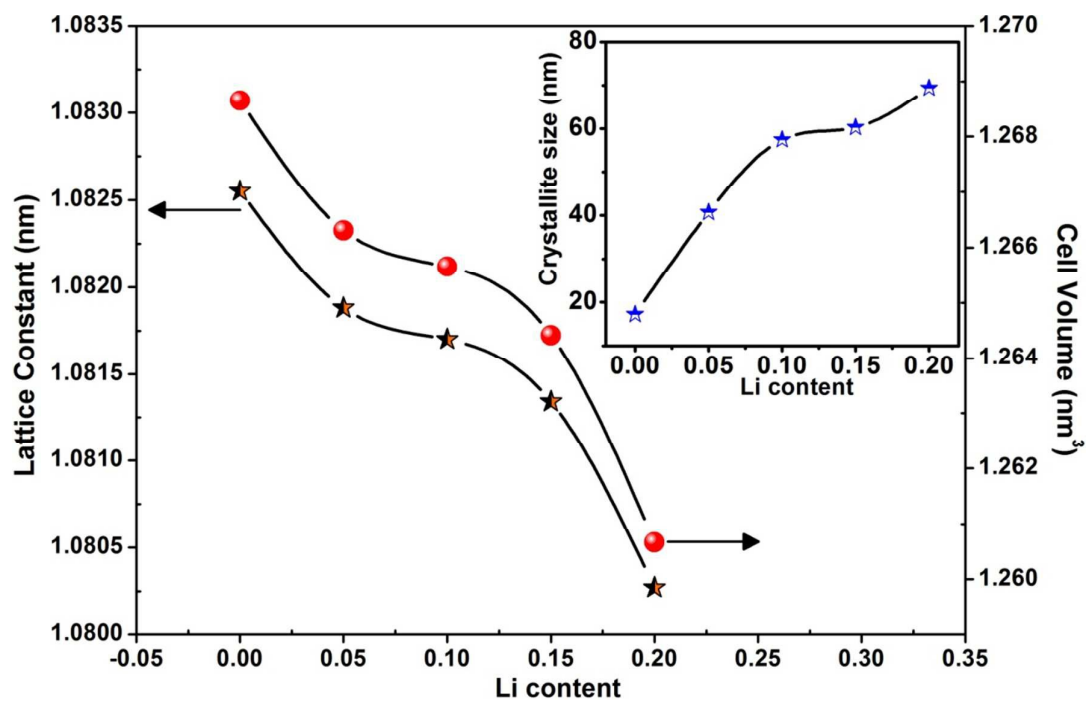


Fig 2. Variation of lattice constant and cell volume of $\text{Gd}_{1.9-x}\text{Eu}_{0.1}\text{Li}_x\text{O}_3$ nanophosphors as a function of lithium content [Inset: crystallite size]

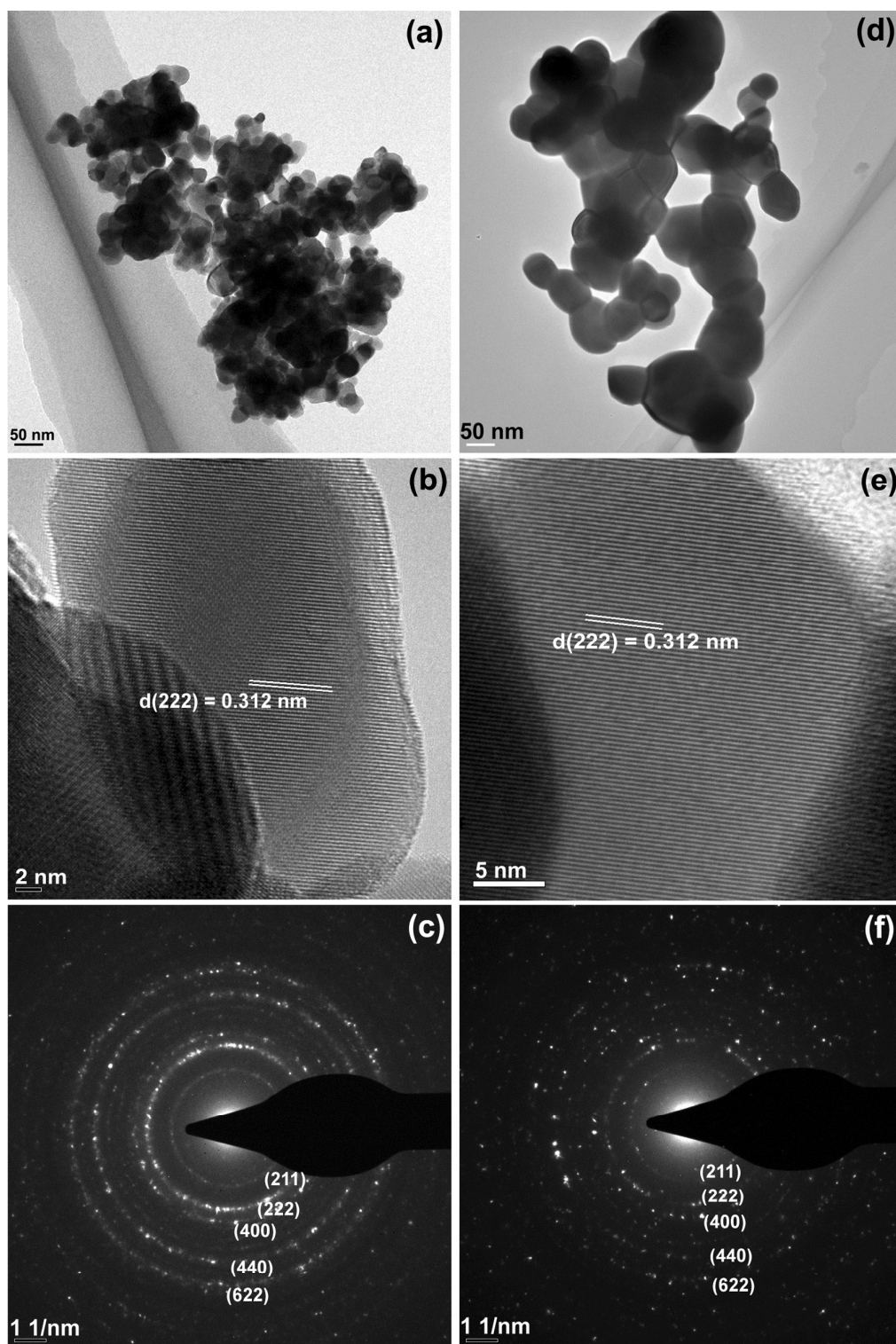


Fig 3. Low and high resolution TEM images and selected area electron diffraction patterns of (a-c) $\text{Gd}_{1.9}\text{Eu}_{0.1}\text{O}_3$ and (d-f) $\text{Gd}_{1.75}\text{Eu}_{0.1}\text{Li}_{0.15}\text{O}_3$ nanophosphors, respectively.

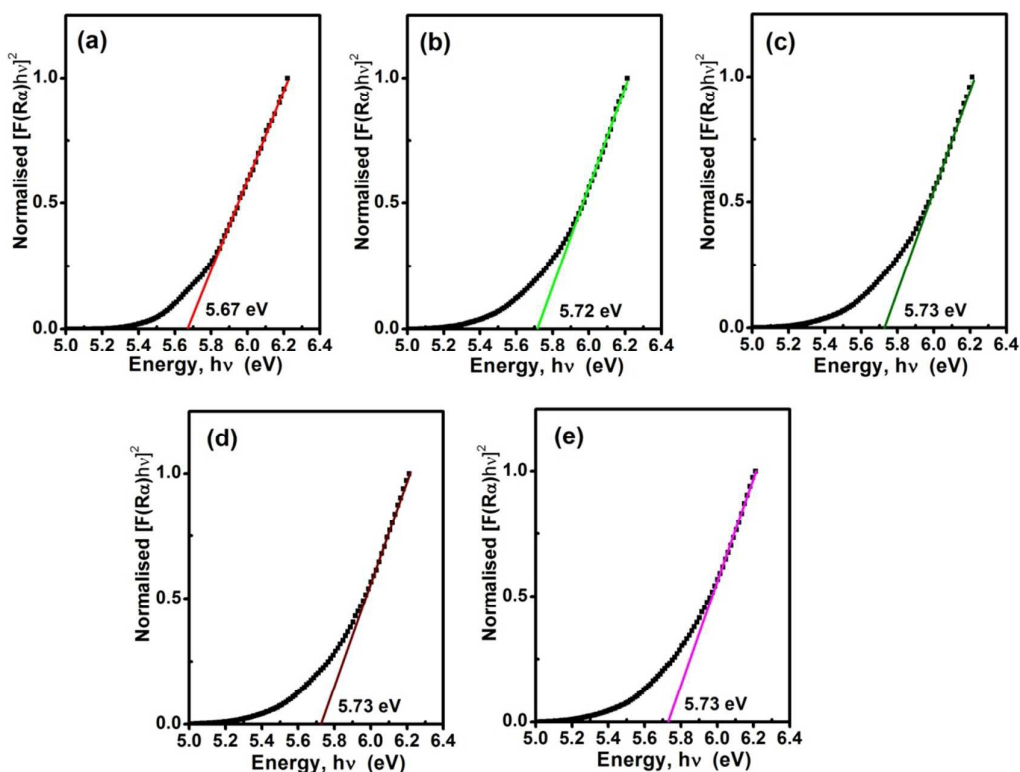


Fig 4. Kubelka-Munk plots of $\text{Gd}_{1.9-x}\text{Eu}_{0.1}\text{Li}_x\text{O}_3$ nanophosphors with different Li^+ content (x): (a) 0, (b) 0.05, (c) 0.1, (d) 0.15 and (e) 0.2.

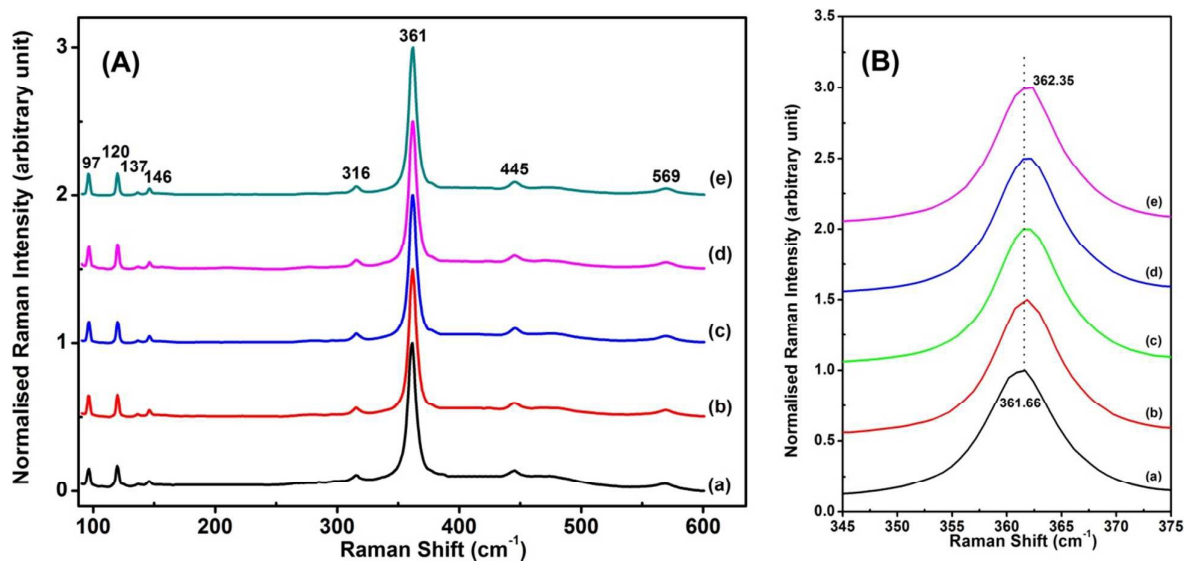


Fig 5. Normalised microRaman spectra of $\text{Gd}_{1.9-x}\text{Eu}_{0.1}\text{Li}_x\text{O}_3$ nanophosphors with different lithium content (x): (A)- (a) 0, (b) 0.05, (c) 0.1, (d) 0.15 and (e) 0.2 and (B) Magnified Raman spectrum in the neighbourhood of the peak at 362 cm^{-1} .

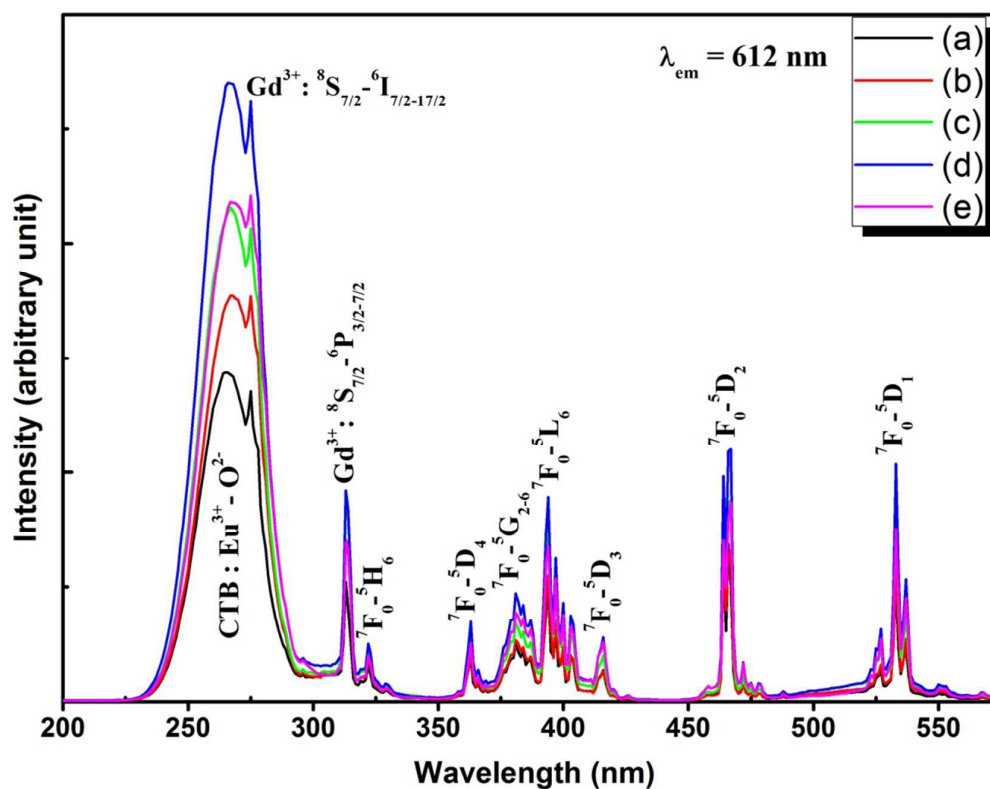


Fig 6. Excitation spectra of $\text{Gd}_{1.9-x}\text{Eu}_{0.1}\text{Li}_x\text{O}_3$ nanophosphors ($\lambda_{\text{em}}=612$ nm) with different Li^+ content (x): (a) 0, (b) 0.05, (c) 0.1, (d) 0.15 and (e) 0.2.

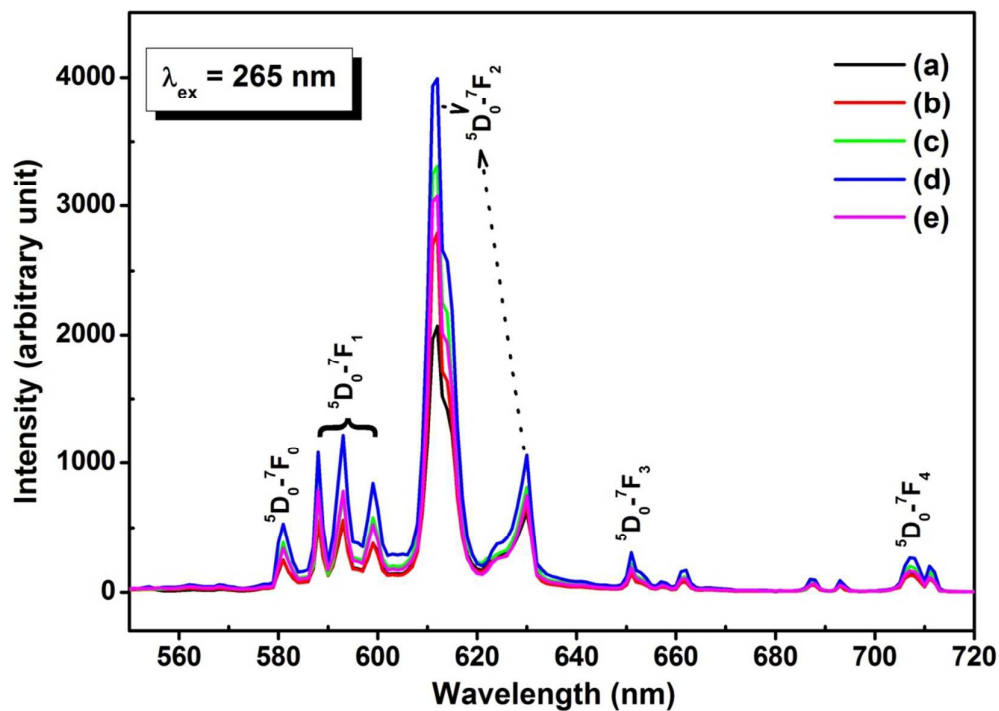


Fig 7. Emission spectra of $\text{Gd}_{1.9-x}\text{Eu}_{0.1}\text{Li}_x\text{O}_3$ nanophosphors ($\lambda_{\text{ex}}=265$ nm) with different Li^+ content (x): (a) 0, (b) 0.05, (c) 0.1, (d) 0.15 and (e) 0.2.

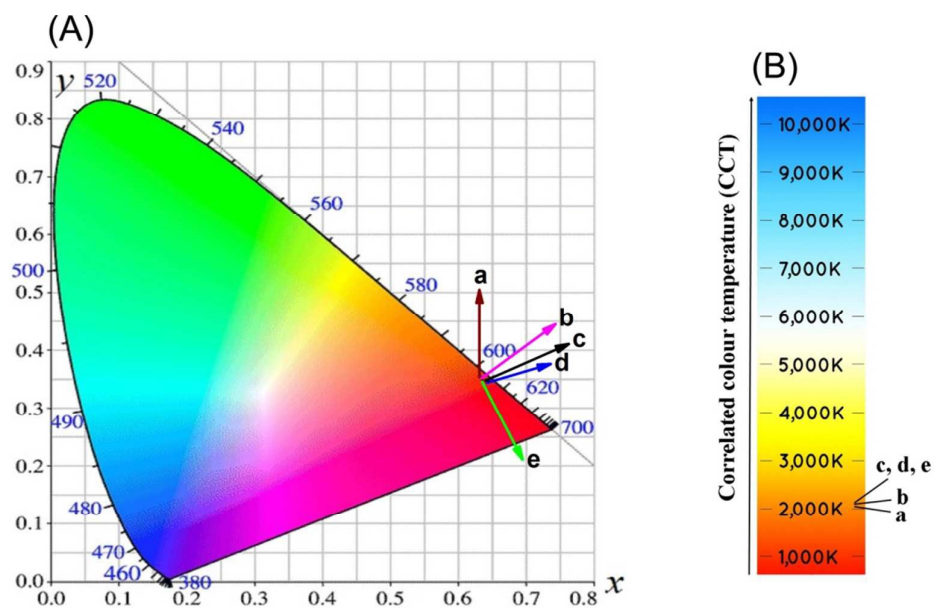


Fig 10. (A) CIE chromaticity diagram and (B) correlated colour temperature diagram of $\text{Gd}_{1.9-x}\text{Eu}_{0.1}\text{Li}_x\text{O}_3$ nanophosphors with different Li^+ content (x): (a) 0, (b) 0.05, (c) 0.1, (d) 0.15 and (e) 0.2.

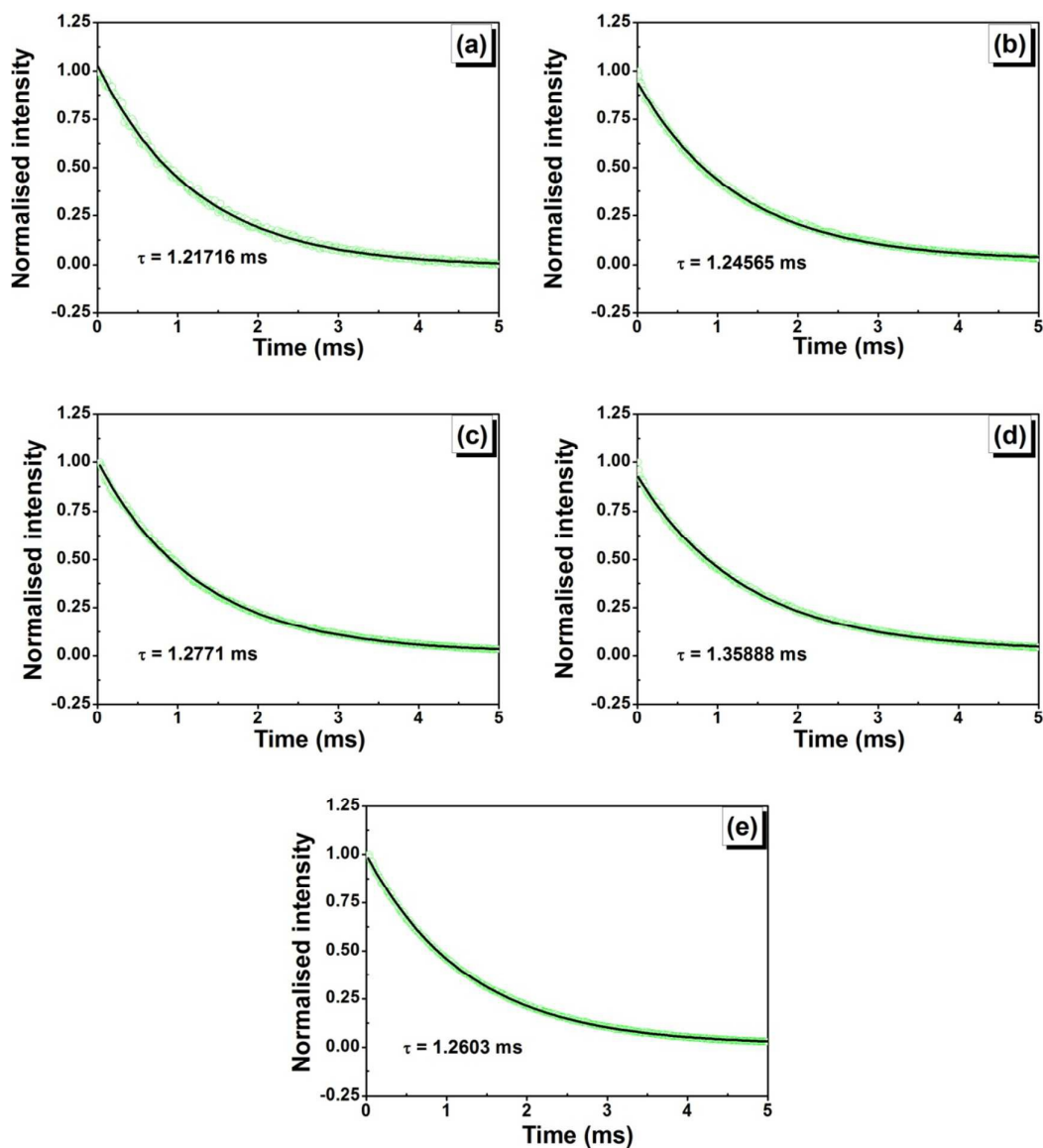


Fig 11. Luminescence decay curves of Eu^{3+} (${}^5\text{D}_0 \rightarrow {}^7\text{F}_2$ transition at 612 nm, $\lambda_{\text{ex}}=265$ nm) in $\text{Gd}_{1.9-x}\text{Eu}_{0.1}\text{Li}_x\text{O}_3$ with different Li^+ content (x): (a) 0, (b) 0.05, (c) 0.1, (d) 0.15 and (e) 0.2 (experimental data (o) and fitting results (-)).

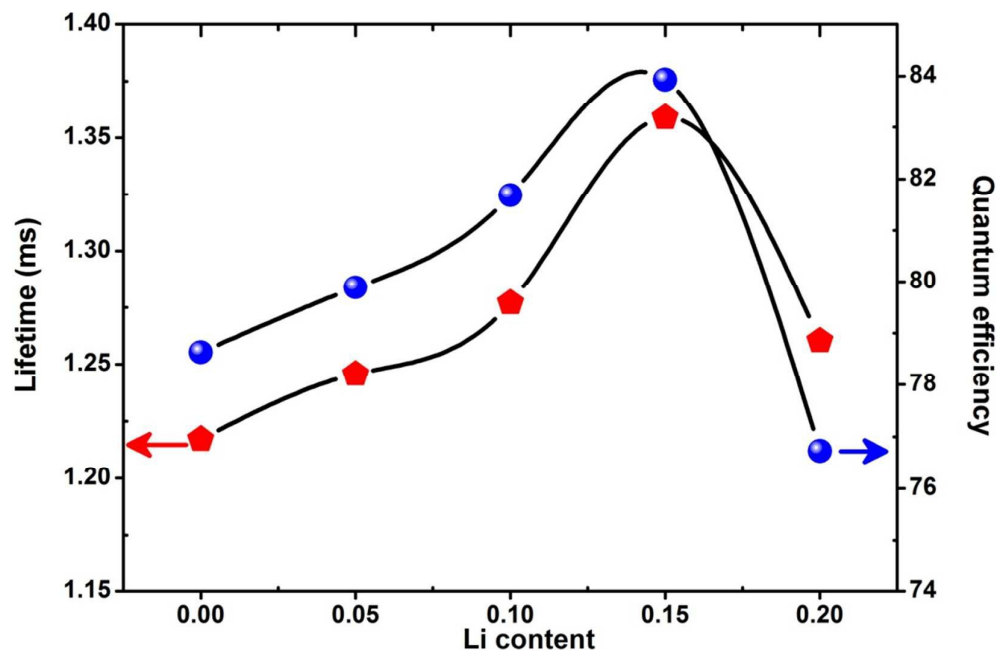
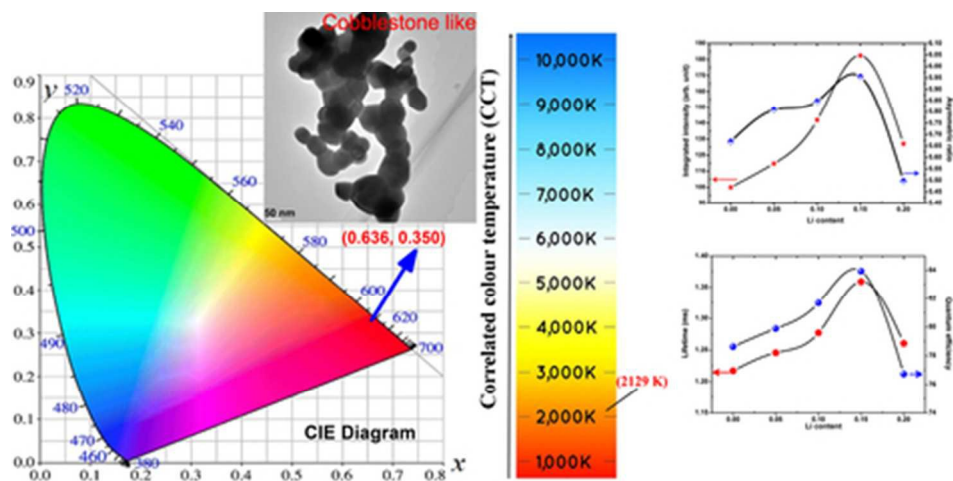


Fig 12. Variation of lifetime and quantum efficiency of $\text{Gd}_{1.9-x}\text{Eu}_{0.1}\text{Li}_x\text{O}_3$ nanophosphors as a function of Li^+ content.

Graphical abstract (One sentence)

Highly luminescent Li⁺ ion compensated Gd₂O₃:Eu³⁺ nanophosphors, a potential candidate for photonic applications



39x19mm (300 x 300 DPI)